Oxygen Induced faceting of the Chiral (531) surface of Platinum

Matthew Seithel

Physics MSci

1st Supervisor: Prof I Robinson

2nd Supervisor: Prof D McMorrow

Abstract

The (531) chiral surface of platinum was exposed to oxygen during heating to cause faceting and the surface studied by Surface X-ray Diffraction on the B16 beamline at Diamond Light Source. The integrated intensity of crystal truncation rods was calculated to analyze the surface and it was found that faceting had occurred, and the surface relaxation from the asymmetry of CTR profiles was positive.

Contents

Aims

This experiment set out to observe oxygen induced faceting of the Pt(531) chiral surface in real time, by in situ heating of the crystal whilst observing by surface X-ray diffraction.

Equilibrium Crystal Shapes

Perfect crystals in perfect equilibrium will have a shape determined only by the energy required to form a crystal/vapour boundary in a direction with respect to the crystal's orientation.[1] This is the fundamental premise of the Theory of Equilibrium Crystal Shapes, and one which is useful when approaching single-crystal study. The theory states that the shape of the crystal is determined by minimizing the surface integral of the interfacial free energy density, resulting in an expression which leads to the Wulff construction as a function of crystal orientation.[2]

Assuming the surface tension, γ, to be isotropic, a finite volume body will reduce its surface energy to a minimum, which for an isolated body, would result in a sphere. For crystals, however, the surface tension is a function of crystal orientation also, $\gamma(n)$, as in Fig 1.

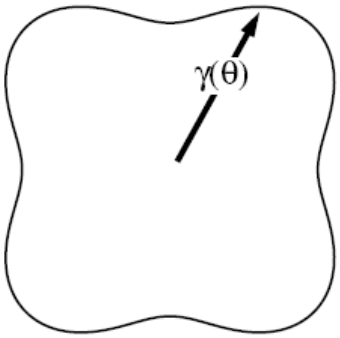

[1] Phys. Rev. B **24**, 6274, (1981)
[2] Met. Trans. A, pp 1431, (1996)..

Fig 1- An example of surface tension as function of orientation, n, of a surface

The Wulff construction, representing the surface free energy, is found by drawing a ray from the origin to the surface of $\gamma(n)$, and at the end of each ray constructing the perpendicular half plane. The interior of the envelope that results from all half planes is the minimizing shape for a finite isolated volume. Fig 2. Mathematically equivalent is the solution of the equation:

$R(\theta) = \min (\gamma(n))/(n\cdot \theta)$ [3]

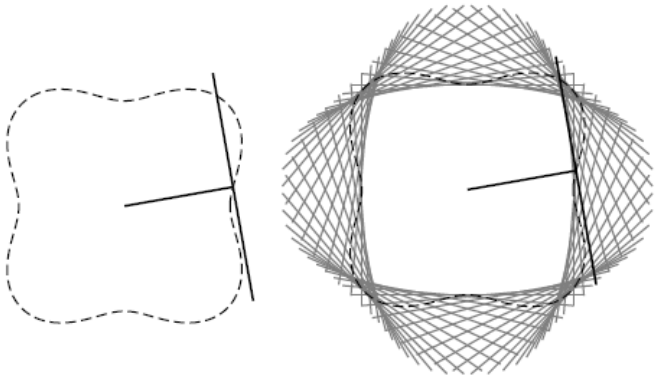

Fig 2- Wulff construction used to calculate the minimizing surface for a fixed volume with anisotropic surface tension.

It is easy to see that a strong dependence on the orientation of the crystal will result in much more complex surface tension distributions than those demonstrated in Figs 1 & 2. The surface tension distribution in real- life systems involve more extensive variation with respect to orientation, with areas of high tension directly adjacent to low-tension regions due to the orientation of the crystal. An example such as that in Fig 3 shows the

[3] Phys. Rev. Lett. **75**, 2968, (1995)

significance of the minima of the surface tension (surface free energy), as it is at these cusps, which the minimized shape forms a flat face, or facet.[4]

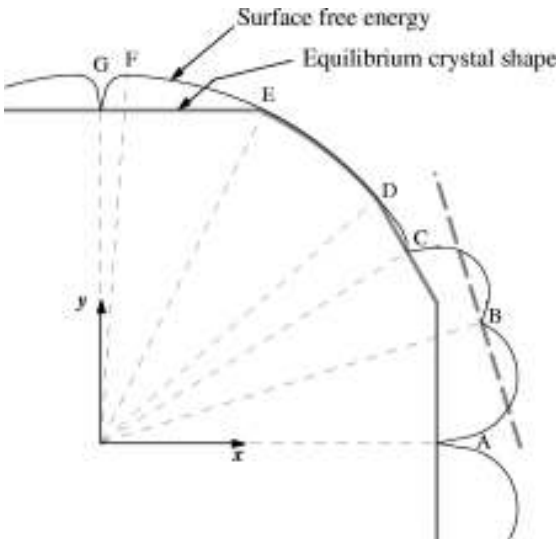

Fig 3- Wulff construction showing relationship of minima and facets

It is clear, however, that surface free energy is highly dependant upon the temperature of the crystal; at very high temperature, the equilibrium shape of the crystal will be spherical, but as it cools, the minima in surface free energy will give rise to facets. These facets will form at orientations with lower surface free energy than adjacent orientations, at the point where it benefits the surface energy to do so. Facets will change in area as a function of temperature, as during heating, more of the surface will become microscopically rough, while during cooling, the rough surface will split into facets. The point, at a particular orientation, when the surface becomes rounded during heating, is called the roughening transition. Equally, the same boundary forming facets during cooling is also a roughening transition, but from the other perspective.

In the case of high miller-index crystal surfaces, the crystal is flat in the surface direction because it has been cut and polished to be so. When heated up to the region of the

[4] Phys Rev B **64**, 045412 (2001)

roughening transition, the surface mobility will increase, often changing from a high surface free energy orientation, to a combination of lower surface free energy adjacent orientations.[5] This has been demonstrated on metal surfaces, notably Cu(115) by Walko & Robinson[6] , showing the formation of facets upon heating in the presence of oxygen.

For Platinum, the roughening transition occurs at close to 1000K, as the atoms are freer to move and are able to reconstruct on the surface. This is a significantly lower temperature than the melting point of Pt, which is 2041K. Starting at a low temperature with the Pt(315) surface, the heating effect will increase surface mobility up until the region of 1000K, at which point the roughening transition is expected to cause reconstructions on the surface, resulting in the formation of facets.

Diffraction

The study of crystals by X-ray diffraction is a well developed method, useful because when the wavelength is comparable to the lattice constant, the beam can be diffracted in directions entirely different to the incident direction. The Bragg derivation for diffracted beams from a crystal is fairly straightforward, treating each layer of the lattice as a partially silvered mirror plane, and the constructive and destructive interference arising from the path length difference between layers gives rise to the peaks in intensity.

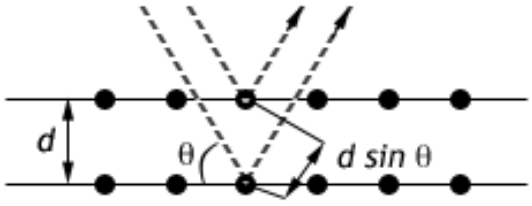

Fig 4- Bragg diffraction model

[5] Phys. Rev. Lett. **50**, 2017 (1983)
[6] Phys. Rev. B **64**, 045412 (2001)

For lattice planes with spacing, d, and an incident beam of wavelength λ at an angle θ to the plane, the path length difference and corresponding diffraction condition is given in the Bragg law,

$2d \sin\theta = n\lambda$

This derivation is useful because it returns correct results, but it is very simplistic. In order to understand diffraction one must look beyond the contribution of the simple periodicity of the lattice and find the scattered amplitude from the basis, i.e. from the electron density within the cell. The periodicity of the lattice makes Fourier analysis an ideal method of describing the electron number density effectively and hence finding the scattered amplitude arising from the basis. Knowing that the electron number density, $n(\mathbf{r})$, is periodic,

$$n(\mathbf{r} + \mathbf{T}) = n(\mathbf{r})$$

the electron number density can be described in one direction (x) as a Fourier series of sines and cosines:

$$n(x) = n_0 + \sum_{p>0} [C_p \cos(2\pi px/a) + S_p \sin(2\pi px/a)]$$

where p are positive integers and C_p, S_p are Fourier coefficients (real constants). In a compact exponential form, this reduces to:

$$n(x) = \sum_p n_p \exp(i2\pi px/a)$$

in which the sum is now over all p.

The coefficients n_p are now complex, so to ensure that the function n(x) is real, we must require that

$$n^*_{-p} = n_p$$

Extending the one-dimensional calculation to a three dimensional crystal gives an expression involving a new set of vectors, **G**:

$n(\mathbf{r}) = \sum_G n_{\mathbf{G}} \exp(i\mathbf{G} \cdot \mathbf{r})$

This new set of vectors must be invariant under crystal transformations which leave the crystal unchanged, i.e **T**. The Fourier coefficients in the expression, n_p are given by the relation

$n_p = a^{-1} \int^{a}_{0} dx\, n(x) \exp(-i2\pi px/a)$

in full, this is

$n_p = a^{-1} \sum_p n_{p'} \int^{a}_{0} dx \exp[i2\pi(p'-p)x/a]$

Generalising this to the three dimensional equation,

$n_G = V_c^{-1} \int_{cell} dV\, n(\mathbf{r}) \exp(-i\mathbf{G} \cdot \mathbf{r})$

Here V_c is the volume of the cell in the crystal. The nature of the vectors G of the Fourier sum can be found by constructing the axis vectors of the reciprocal lattice.

$b_1 = 2\pi\, (a_2 \times a_3)/(a_1 \cdot a_2 \times a_3)$

$b_2 = 2\pi\, (a_3 \times a_1)/(a_2 \cdot a_3 \times a_1)$

$b_3 = 2\pi\, (a_1 \times a_2)/(a_3 \cdot a_1 \times a_2)$

These form the axis vectors of the reciprocal lattice, upon which reciprocal lattice vectors, G, are mapped.

From this derivation comes a more complete understanding of diffraction, when we look at the relation of the reciprocal lattice vectors G to the wavevectors of the incident and outgoing waves. For an incident wave with wavevector **k** and an outgoing wave with

wavevector **k'**, the difference in phase factors is exp[i(**k - k'**) · **r**]. The condition for constructive interference, then, is

$$\exp[i(\mathbf{k} - \mathbf{k'}) \cdot \mathbf{r}] = 1$$

which leads to a comparison with the previous equation for Fourier coefficients. If

$$\mathbf{k} - \mathbf{k'} = \Delta\mathbf{k}$$

$\Delta\mathbf{k}$ is the scattering vector. It is readily apparent that in the expression for scattering amplitude,

$$F = \sum_G \int dV \, n_G \exp[-i(\mathbf{G} - \Delta\mathbf{k}) \cdot \mathbf{r}]$$

that if the scattering vector is equal to the reciprocal lattice vector,

$$\Delta\mathbf{k} = \mathbf{G}$$

then the exponential vanishes and the scattering amplitude is just $F = n_G V$. Since the scattering is elastic, so the magnitude of k and k' are equal. Hence the diffraction condition is given by

$$2\mathbf{k} \cdot \mathbf{G} + G^2 = 0$$

and since if G is a reciprocal lattice vector, so then is –G, the condition can be written as

$$2\mathbf{k} \cdot \mathbf{G} = G^2$$

In order for diffraction to occur, the scattering vector $\Delta\mathbf{k}$ must align along a reciprocal vector G. All of the possible scattering vectors can be represented in the Ewald construction as radial vectors, overlaid on a map of reciprocal space with reciprocal lattice points, some of which will be intersected by the resultant sphere. The use of a sphere in the Ewald construction is helpful in demonstrating the conditions required for diffraction to occur in all three dimensions.

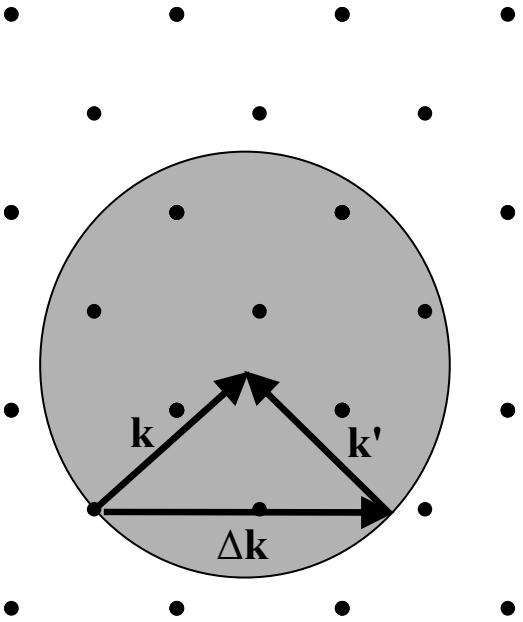

Fig 5- Ewald construction

If the reciprocal lattice vector is given by

$\mathbf{G} = h\mathbf{b_1} + k\mathbf{b_2} + l\mathbf{b_3}$

then the coefficients, h,k,l, are the miller indices of the reciprocal lattice.

$h = b_1 a/2\pi$

$k = b_2 a/2\pi$

$l = b_3 a/2\pi$

where a is the lattice constant. The Laue condition states that h, k, and l must simultaneously be integers for diffraction from a bulk crystal to occur.

Surface diffraction and CTRs

Surface X-ray Diffraction has grown to be an extremely useful method for analyzing crystal surfaces, as information about the surface itself can be extracted from the diffraction patterns obtained. The basis for this is the truncation of the crystal at the surface introducing discontinuity into the scattered amplitude, so by studying the part of

the scatter due to the truncation, information about the properties of the surface can be found.

The surface of the crystal introduces diffuse scattering features perpendicular to the surface in reciprocal space, as described by the equations below.

The electron density of the crystal in the bulk is the electron density of the unit cell, combined with a series of delta functions representing the lattice points.

$\rho_{crystal}(r) = \rho_{cell}(r) \sum^{+N}_{-N} \delta (x - n_1a) \delta(y - n_2b) \delta(z - n_3c)$

when the crystal truncates, one of these delta functions (usually the third) no longer contributes, meaning the scattered amplitude is altered:

$A \alpha \sum^{N}_{-\infty} F_{bulk} \exp(-in\mathbf{q}.\mathbf{c})$

$= F_{bulk} (\exp(-iN\mathbf{q}.\mathbf{c})/(1-\exp(-i\mathbf{q}.\mathbf{c}))$

and the intensity is

$$I \ |A|^2 \ \alpha |F_{bulk}|^2 \frac{1}{4\sin^2\left(\frac{q \cdot c}{2}\right)}$$

This predicts high intensity at the Bragg peaks, as expected, but away from the peaks, the intensity does not go to zero. Rather the diffracted intensity appears as rods perpendicular to the surface intersecting the bulk peaks for h and/or k not equal to zero. The intersection of these rods with the Ewald sphere allows their intensity to be measured.

Pt (531) surface

In order to use surface X-ray diffraction on this surface, it is necessary to find a coordinate transformation matrix from the bulk structure frame to the (531) surface frame. The surface can be viewed as a stepped edge in the bulk frame, represented in Fig 6, where each layer of points overlays the sublayer. This is a simple cubic representation of the surface in real space.

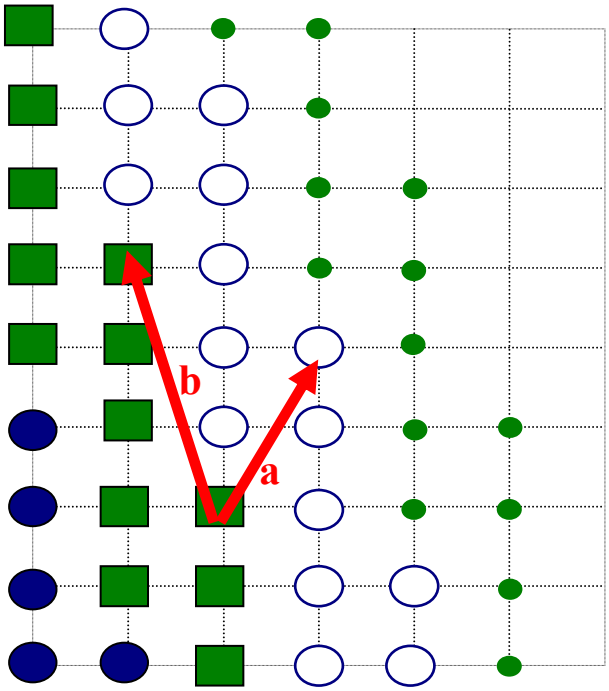

Fig 6- (531) surface representation with surface vectors drawn in red, blue circles showing topmost layer, green squares next layer, hollow circles third layer etc.

In Fig 6 the vectors drawn on the diagram are non-collinear vectors down the step (a), along the step edge (b), and the surface normal(c). And because these steps in the surface frame correspond to the (100),(010),(001) steps, the matrix can be constructed.

a = (1,2,-1)

b = (-1,3,0)

c = (3 ,1,5)

a x b = (3 , 1 , 5)

b x c = (15, 5, -10)

c x a = (-11, 8, 5)

$$M_{315}=\begin{pmatrix}1 & -1 & 3\\ 2 & 3 & 1\\ -1 & 0 & 5\end{pmatrix} \qquad M^{-1}{}_{315}=\frac{1}{35}\begin{pmatrix}15 & -11 & 3\\ 5 & 8 & 1\\ -10 & 5 & 5\end{pmatrix}$$

The change of indices so that the high index, 5, lies along the L direction is simply a convention.

Method

The experiment was carried out on the B16 beamline at Diamond Light Source from the 25th Feb 09 – 2nd March 09. Delays and incompletion in the manufacturing of the crucial "baby-chamber" caused the moving of the run from January to the end of February.
In order for the faceting to be observed in real time, a chamber was planned and ordered which would allow heating to high enough temperatures to cause faceting, whilst being in position on the beamline, with a beryllium cover to allow study by X-ray diffraction during the heating process. This chamber was delayed in manufacture, and had still not been completed at the time of the experiment, so the aims of the project were adjusted. The sample was prepared before observation, put under the conditions in which faceting

was expected, and then transferred to the beamline for observation. In this way, the faceting effect could be studied, but not in real time.

The B16 beamline at Diamond (Fig 7) operates in the photon energy range 4-20keV for monochromatic X-rays, and is used for testing out new optical components and detectors as well as "exploratory" experiments from external users[7].

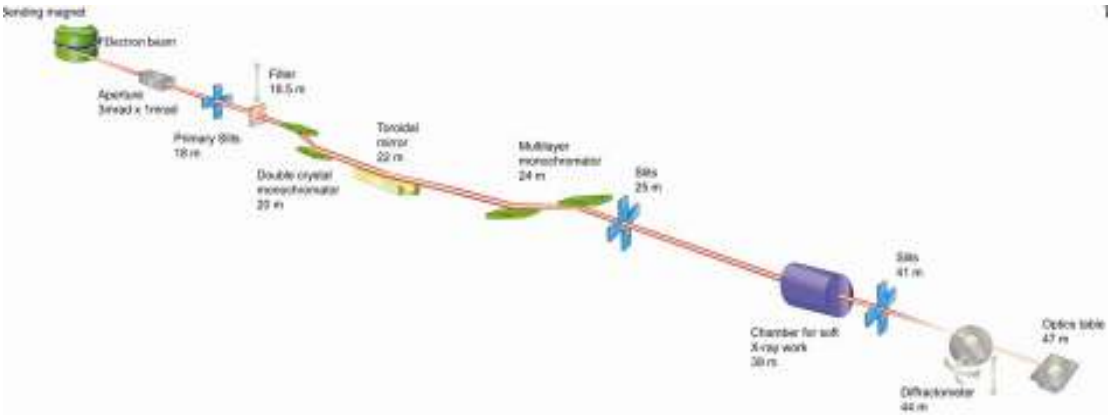

Fig 7- B16 beamline schematic

The adaptability of this beamline made it ideal to try out a new "in situ" technique of faceting observation. The beamline is equipped with a Huber 5-circle diffractometer, which is essentially a 4-circle Huber 5020 diffractometer, shown in Fig 8, with a delta axis added onto the structure for more degrees of freedom.

[7] www.diamond.ac.uk/Beamlines/Beamlineplan/B16

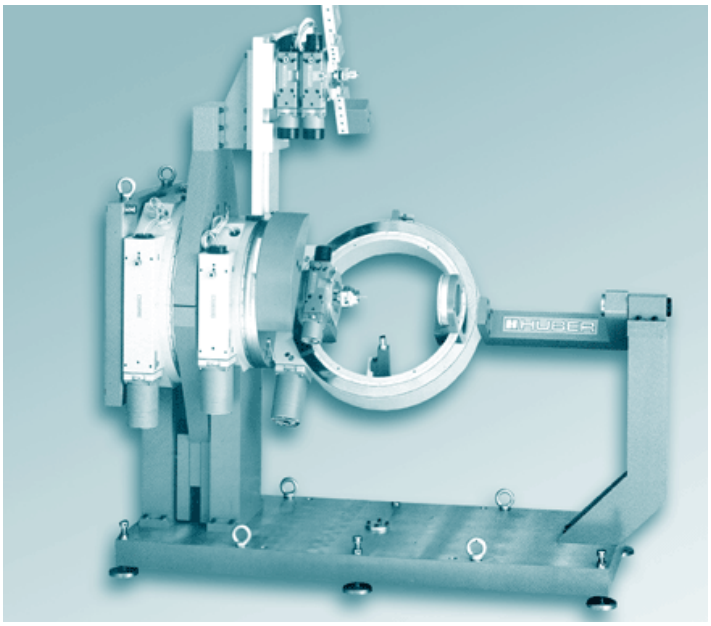

Fig 8 Huber diffractometer

The 5-circle Huber diffractometer allows the detector and sample to be rotated to a wide range of angles and orientations, so alignment of this was the first objective of the experiment. The angles were set to zero and the beam aligned with the X-ray eye detector. The movement of the diffractometer, slits, and detector were all controlled by either the EPICS interface or GDA. EPICS (Experimental Physics and Industrial Control System) is a lower level program controlling the hardware of the beamline, so this was used to align the diffractometer and beam. GDA (Generic Data Acquisition) software was used later in the experiment to provide GUI and enable scannables. The interaction between the user and the equipment motors is facilitated by several layers of programs, as demonstrated in Fig 9.

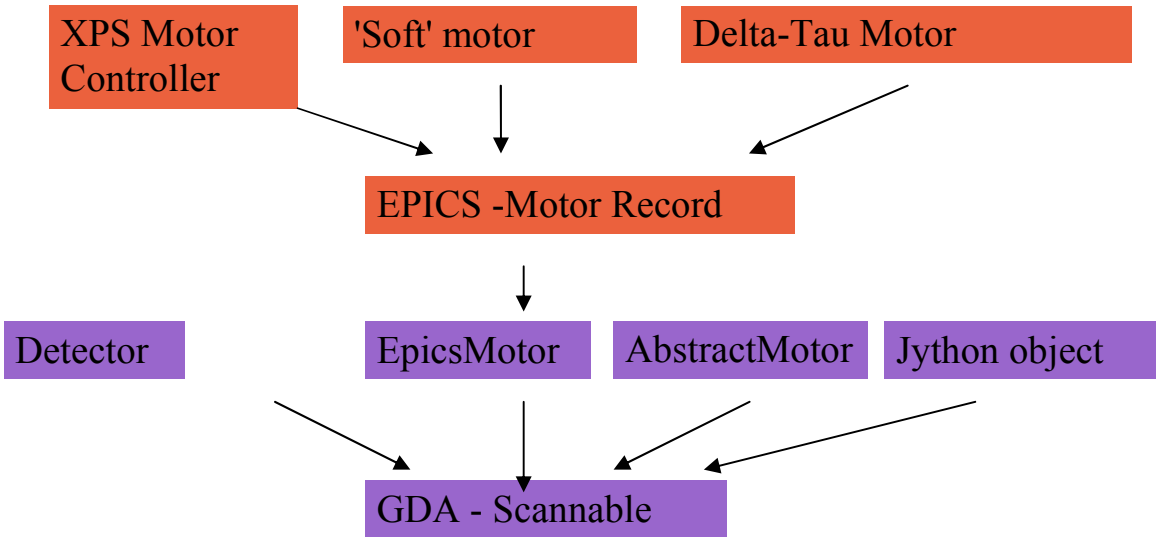

Fig 9- Interaction of motors with GDA

A pin was installed in the diffractometer stage at the height of the sample, such that the tip would align with the position of the sample once it was installed. The offsets necessary to centre the tip with the X-ray eye were:

X centre = +1.02 mm

Y centre = +1.06 mm

Base diffractometer: X= -2.97 mm

Height = -26.7 mm

Pitch = -0.312˚

Sample Stage: X= -0.345mm

Y= +0.545mm

Z= -11.8 mm

The energy of the beam was set to 11.3 keV, just below fluorescence, and an extra set of slits was mounted after the sample, before the detector. These slits, S6, were aligned as in Fig 10, with an offset X = -0.71 mm.

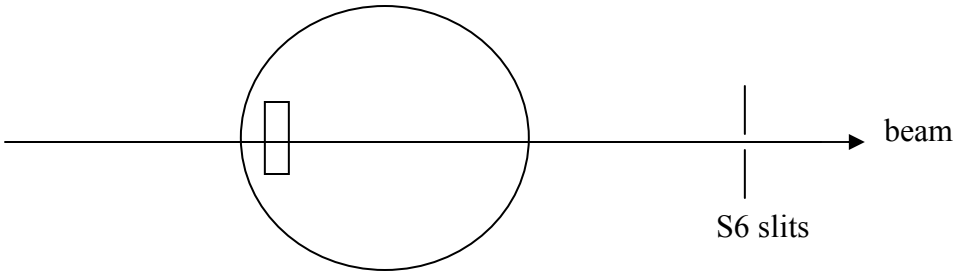

Fig 10- Detector slits, S6

For the beam to pass straight through, an α offset of α =-0.277˚ is needed. Hence this was adjusted in EPICS so that α =0 allows straight-through beam.

Having finished alignment of the diffractometer, the sample was installed on the sample stage, and alignment for this started. The initial alignment was done by laser, with offsets of φ = 69˚, χ = 1.9˚. The crystal alignment, and finding of the UB matrix was done through the GDA interface by finding Bragg peak reflections and optimising their positioning in φ and χ.

The UB matrix is the product of the U matrix (orientation matrix) and the B matrix (material matrix). GDA incorporates code which calculates the UB matrix from two Bragg peak reflections, if they can be identified and optimized. Hence once the sample was aligned perpendicular to the sample holder by laser, the diffractometer could be moved in reciprocal space to the bragg reflections. The [-1, -2, 7] peak was found at 121.37˚ in phi and 44.4˚ in chi after optimising in phi and chi until it reached a maximum. It was necessary to introduce attenuation into the beam in order not to damage the detector when the position became close enough to the Bragg peak to see very high intensity beam. In this process it was important to realize the angular range of the diffractometer was limited to ±140˚ in chi and phi, so certain reflections were unattainable. Several peaks were found, and those used for alignment were [-1,-2,7] and

[0,2,3]. Inputting those into the system with the lattice constants gave a UB matrix shown below.

Crystal

Lattice: a,b,c = 4.80600, 6.20400, 23.21500

Alpha, beta, gamma = 90.00000 , 90.00000, 49.80000

Reciprocal: b1,b2,b3 = 1.71166, 1.32596, 0.27065

Beta1,beta2,beta3 = 1.57080, 1.57080, 2.27242

B matrix: 1.7116647462979 -0.8558515886001 0.0000000000000

0.0000000000000 1.0127635891650 0.0000000000000

0.0000000000000 0.0000000000000 0.270651962403

Reflections

Energy, h, k, l, alpha, delta, omega, chi, phi, tag

1 11.3, -1, -2, 7, 0, 28.0281, 16.7427, 44.6, 116.1750, pt-1-17a

2 11.3, 0, 2, 3, 0, 28.0277, 7.4457, 16.5, -14.76, pt023a

UB matrix

-1.4986346376933 1.2386131916934 -0.001431246571

-0.8262606471176 -0.4732179743084 -0.008668227231

-0.0344059507896 -0.0086104240453 0.270509330934

Sigma: -1.900000

Tau: -68.999993

Wavelength: 1.097205

Energy: 11.300002

Having aligned the sample and configured the system to function entirely in reciprocal space, the detector was installed on the alpha arm.

Pilatus Detector

The Pilatus 100K detector is an area photon counting detector, utilising hybrid pixels and CMOS technology to convert x-ray photons directly to charge, resulting in zero dark current, zero readout noise, and an excellent point spread function.[8] The detector consists of a silicon sensor array bump-bonded to the CMOS- based readout channels, and operates in two basic stages. A preamplifier amplifies the charge created by the x-ray in the sensor material; then a discriminator determines the magnitude relative to a predetermined threshold and produces a digital signal accordingly. This leads into a 20bit counter, which allows completely digital readout and storage of the X-ray count per pixel. [9]

[8] "X-ray imaging with the PILATUS 100k detector"- M. Becha et al. Oct 2007

[9] http://www.aps.anl.gov/Xray_Science_Division/Beamline_Technical_Support/Detector_Pool/Detector_Information/PilatusII_100K/Pilatus100K_DP00221/PSI_Dectris_User_Manual-Pilatus100K-v1_0.pdf

Fig 11- Pilatus 100k detector

With this detector mounted on the diffractometer, images were taken at locations along the crystal truncation rods, giving data in the form of tiff images to be compiled into scans after acquisition.

Rod Scans

Scans were carried out along CTRs at constant h and k, varying l, and exposing for a period of 30s at each point. The first rod scanned was the (11L) rod, scanned either side of the (1 1 9) peak in $\beta_{in} = \beta_{out}$ mode, where the incidence and exit grazing angle are equal. Scans were taken either side of the Bragg peak at (0 2 3), (2 3 2), (-1 0 10), (-1 -2 7) (1 -1 6) in several modes with varying grazing angle.

The sample holder was also connected to a water heater, by which the temperature was raised to 90˚C in order to improve surface mobility. The scans from this series showed little difference to the room temperature scans, the temperature increase not being great enough to modify the surface.

Results and Analysis

The tiff images gathered from the scans were read into the analysis program IGOR Pro, where each rod scan was layered into a movie clip from which further analysis could be done. The images of dimension 487 x 195 pixels simply showed photon count per pixel, and any representation of this within IGOR uses either a grayscale or colormap to illustrate the gradient. Conversion of the 20-bit Pilatus tiff files was required to make them readable in outside programs; this was done within the system using ImageJ before reading them into other data analysis software.

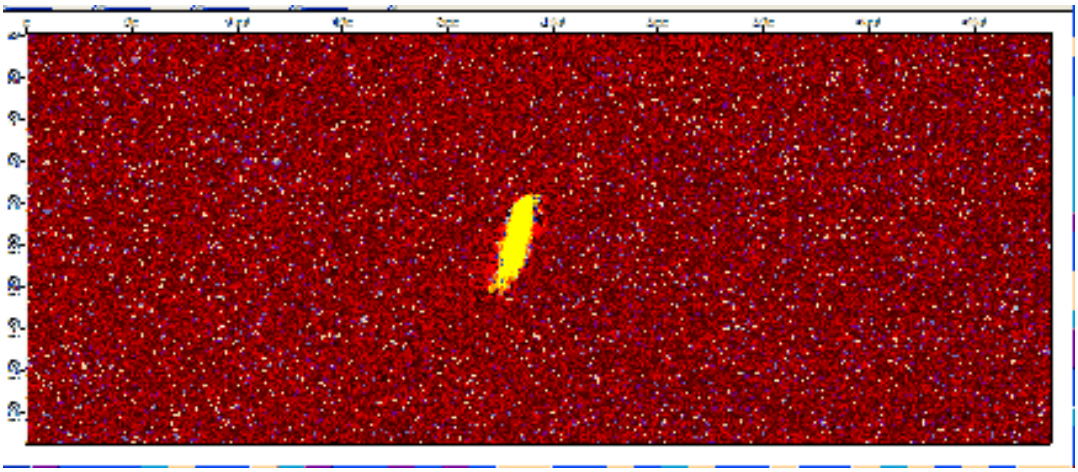

Fig 12- (11L) rod on detector face

The images gathered featured a peak due to the CTR either stationary throughout the scan, or moving across the detector face. Fig 12. As well as this mostly stationary feature, many scans also involved a secondary feature moving across the detector face to coincide with the CTR at the Bragg peak, but moving out of the visible range fairly quickly as L progressed. This is the contribution from the CTR corresponding to the facet, with the coincidence of the Bragg peaks demonstrated by Fig 13 as a function of L.

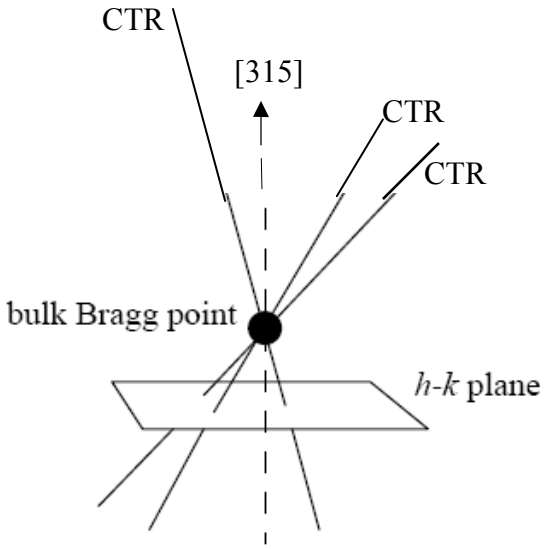

Fig13- Facet CTR's coincidence with Bragg peak

One method of confirming faceting was to centre the facet contribution on the detector and determine the hkl shift as a mechanism to find the facet orientation. This was done on the CTR scan of the (1 -1 6), with the "facet peak" being moved to the centre of the detector.

The centred position was at (0.96 -1.04 5.86)

The difference in h, k and l directly is (-0.04 -0.04 -0.14)

(-4 -4 -14), when transformed by the coordinate (315) matrix is:

$$\begin{pmatrix} 1 & -1 & 3 \\ 2 & 3 & 1 \\ -1 & 0 & 5 \end{pmatrix}\begin{pmatrix} -4 \\ -4 \\ -14 \end{pmatrix} = \begin{pmatrix} -12 \\ -24 \\ -56 \end{pmatrix}$$

This facet peak simplifies to (3 6 14) but the positioning of the peak in the centre of the detector was done manually, and only for this single scan. To get more reliable data, this

would need to be carried out with higher precision on many more scans of different CTRs.

Calculating the integrated intensity of the CTR was done in IGOR by defining a Region of Interest around the feature, as in Fig 14, and plotting its summed intensity in each frame. Comparing the scan position and step size in GDA, the L-position was found for each layer, and the intensity plotted against L.

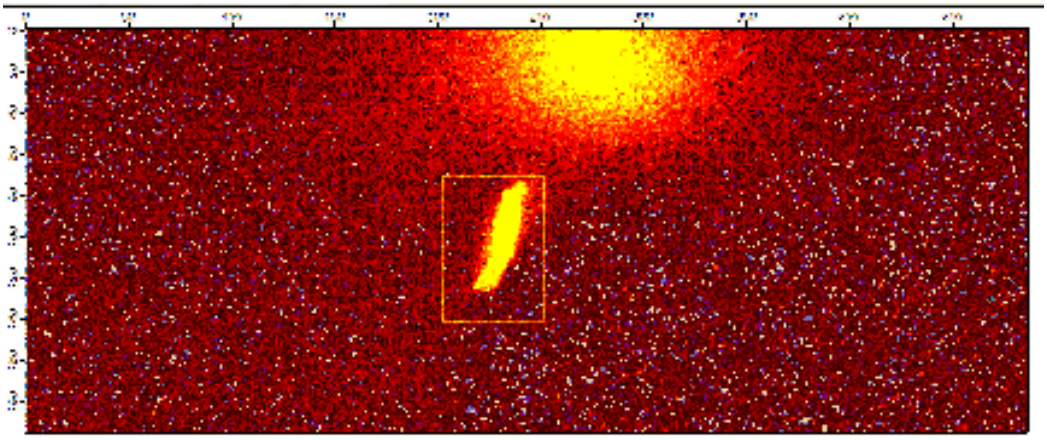

Fig 14- Region of Interest defined around CTR

The integrated intensity of the CTR is only a useful, valid measure when the facet peak feature is not close enough to interfere and distort the intensity. Hence the scans either side of the Bragg peak have been used only up until the point where interference would become a problem. This was done by defining the ROI around the CTR such that the secondary feature was excluded up to the point that the feature became close enough to contribute. The scans were only used up until this point, and the central region overlapping the Bragg peak was left out of the integrated intensity scan.

The resultant integrated intensity profiles for the CTRs around Bragg peaks were plotted, so that the asymmetry of the curves could be seen, as in Fig 15. The profile on either side of the Bragg peaks are not symmetrical, due to reconstruction of the surface affecting the scattering, which can be a useful measure when considering surface relaxation.

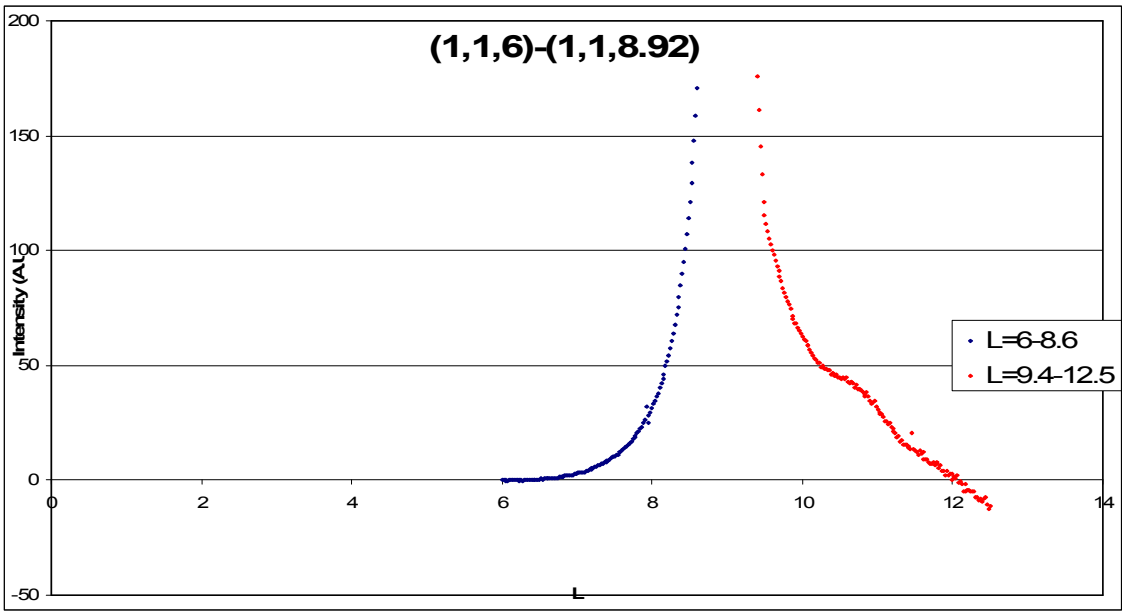

Fig15-Integrated intensity of (11)CTR against L-value (peak at L=9)

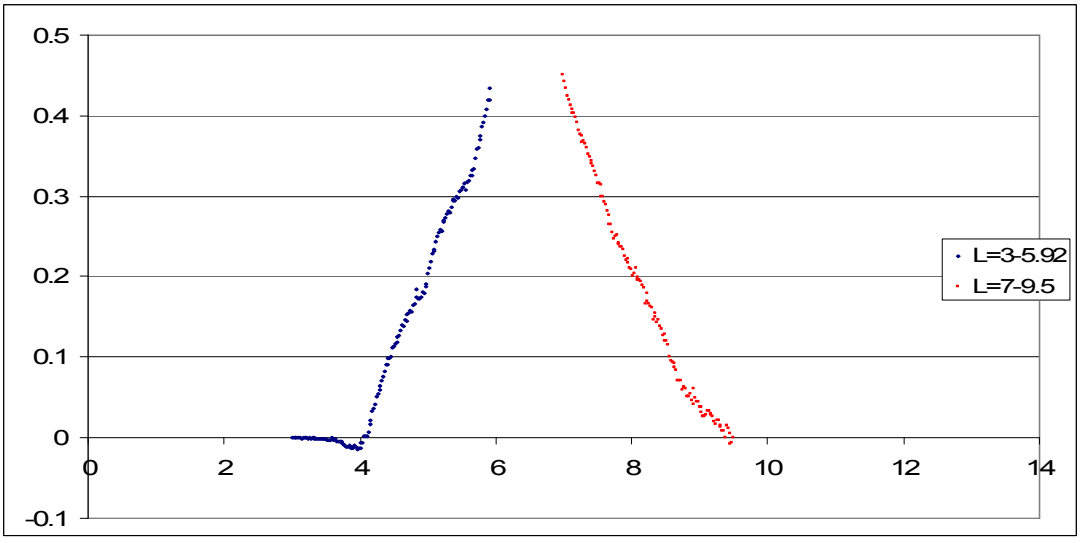

Fig16- Integrated intensity of (1 -1)CTR against L-value (peak at L=6)

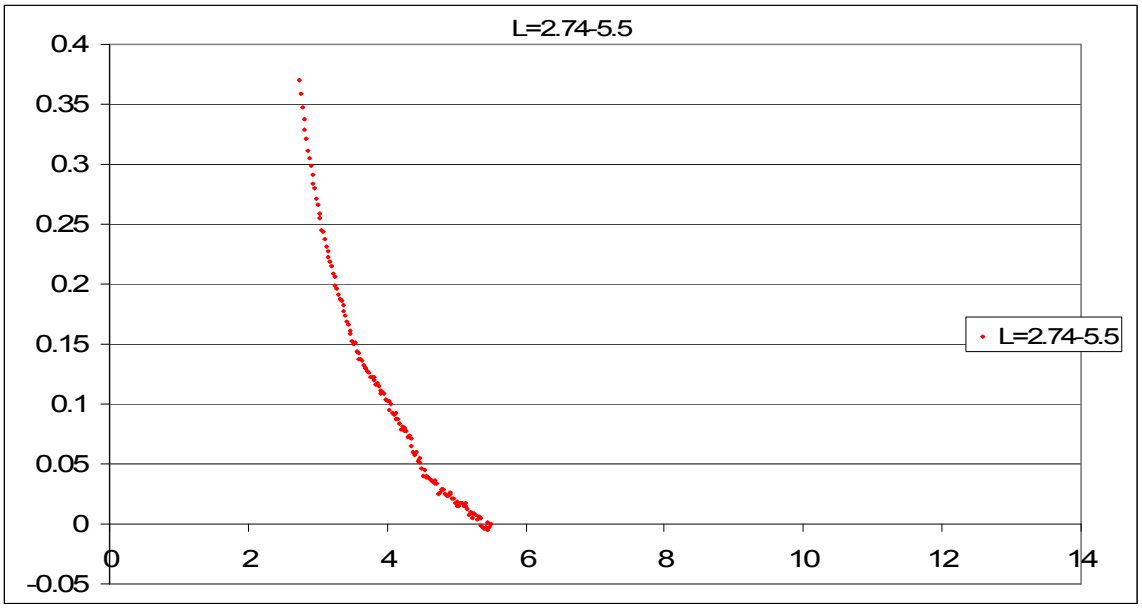

Fig17- Integrated intensity of (2 3)CTR against L-value (peak at L=3)

These scans show the asymmetry increasing as a function of increasing L, pointing towards a positive surface relaxation, i.e. the topmost layers of the surface have expanded, increasing the inter-layer distance. The asymmetry, $\Delta L/L$ is directly proportional to the interlayer distance, and through study of the line shapes, information about the surface relaxation can be extracted. A possible explanation of this is that the oxygen atoms involved in the process, though far too light to contribute to the diffraction, act as a surfactant and cause the Pt layers to expand. The only atoms contributing to diffraction are still the Platinum atoms, but the expansion of the surface layers can be explained by this mechanism.

The log(L-L0) value was also plotted against Log(intensity) for each peak in order to ascertain the surface roughness, as in Fig18.

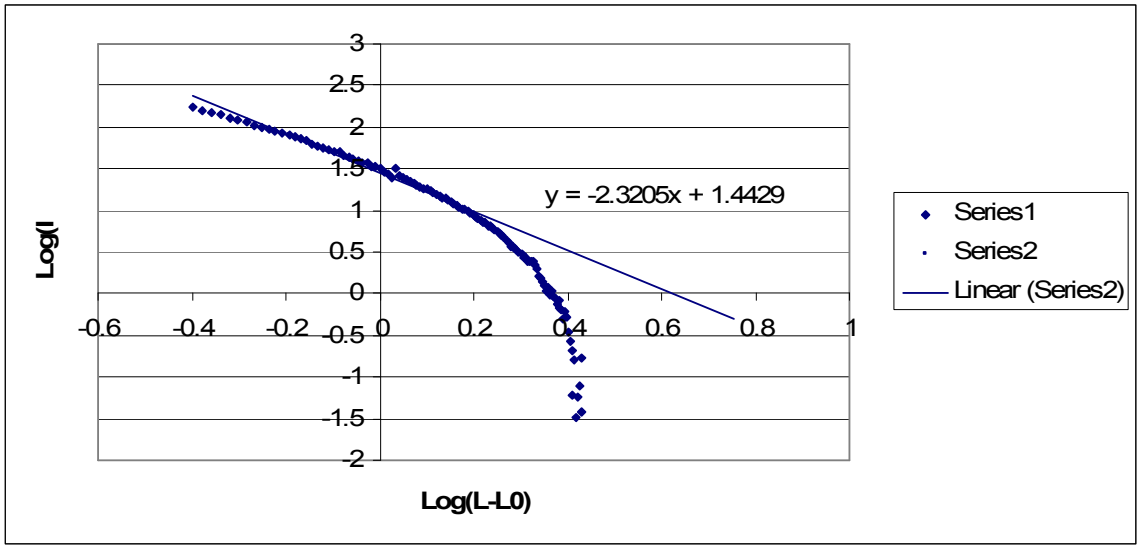

Fig18-Log graph of intensity against distance from peak

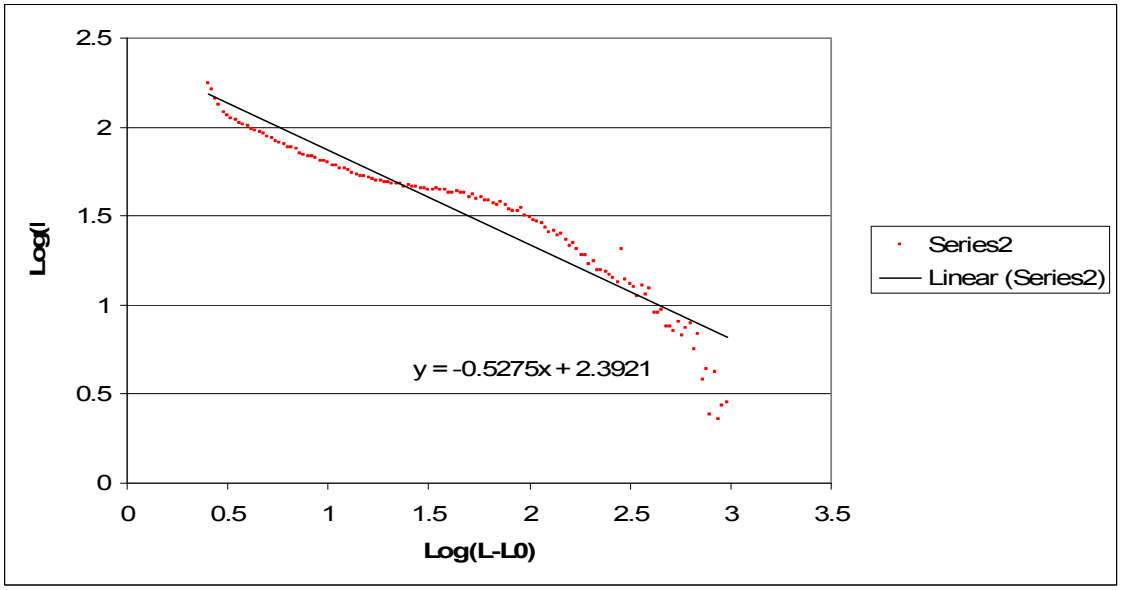

Fig18b- Log graph of intensity against distance from peak

The data found, however, was shown to curve such that any linear fit was unreliable, as well as the intensity being an arbitrary unit. Quantization of the integrated intensity would be required to analyze the data meaningfully, and find a reliable value for the surface roughness.

Conclusion and further study

The project set out to observe, in real time, the process of faceting on the (531) Pt surface. This goal was waylaid by the delay in manufacturing the baby-chamber necessary to accomplish in-situ faceting. However, the surface was shown to have faceted at ~1000K by the existence of facet features in the diffracted intensity as seen by the Pilatus detector. The coincidence of the facet peak with the Bragg peak was seen in almost all scans, and further confirmed the identity of the secondary features. Integrating the intensity of the CTR allowed the surface relaxation to be visualized, and the increasing asymmetry of the rods points towards positive surface relaxation, i.e. expansion of the surface layers. The plotting of logged intensity against distance from the peak did not produce usable results, as the integrated intensity value was arbitrary. Analysis of the surface roughness could be done if the data were quantized correctly. Although some of the aims of this project were fulfilled successfully, the progress was affected by delay and incompletion in manufacture of essential equipment. A great deal more work could be done in this area, as the chiral (531) surface of platinum is yet to be fully understood.

References

*Met. Trans. A, pp 1431, (1996).*J.W. Cahn and W.C. Carter, *Crystal shapes and phase equilibria: A common mathematical basis*,

Phys. Rev. B 24, 6274 (1981): Rottman and Wortis - *Exact equilibrium crystal shapes at nonzero temperature in two dimensions ...*

Phys. Rev. Lett. 75, 2968 - 2971 (1995): V. A. Shchukin, N. N. Ledentsov, P. S. Kop'ev, D. Bimberg - *Spontaneous Ordering of Arrays of Coherent Strained Islands*

Phys. Rev. Lett. 50, 2017 (1983) : C. Jayaprakash, W. F. Saam, and S. Teitel -*Roughening and Facet Formation in Crystals*

Phys. Rev. B 64, 045412 (2001) : D. A. Walko and I. K. Robinson

Energetics of oxygen-induced faceting on Cu(115)

Appl Radiat Isot. 2008 Apr; 66(4) :474-8. Epub 2007 Oct 22 : M. Becha et al. Oct 2007

"X-ray imaging with the PILATUS 100k detector"

http://www.aps.anl.gov/Xray_Science_Division/Beamline_Technical_Support/Detector_Pool/Detector_Information/PilatusII_100K/Pilatus100K_DP00221/PSI_Dectris_User_Manual-Pilatus100K-v1_0.pdf

Springer Verlag, Berlin, (1988), Vol. VII, pp. 367-406. (Chapter 13) : M. Wortis,

"Equilibrium crystal shapes and interfacial phase transitions," in Chemistry and Physics of Solid Surfaces, edited by R. Vanselow

Appendix1- Clarification of role

I was involved in the faceting experiment itself at Diamond Light Source, being familiar with the GDA and EPICS interfaces from my time at Diamond in summer 2008, I was able to help with alignment, run scans, convert images and compile data. After the experiment, I worked in IGOR Pro integrating intensities of the crystal truncation rods, and compiling the report.